



Amorphizing noble metal chalcogenide catalysts at the single-layer limit towards hydrogen production

Yongmin He^{1,2,3,20}  , Liren Liu^{4,5,20}, Chao Zhu^{2,6,20} , Shasha Guo^{2,20}, Prafful Golani², Bonhyeong Koo⁷, Pengyi Tang⁸, Zhiqiang Zhao⁵, Manzhang Xu^{2,9} , Chao Zhu² , Peng Yu¹⁰, Xin Zhou¹¹, Caitian Gao¹², Xuewen Wang¹⁰ , Zude Shi¹, Lu Zheng⁹, Jiefu Yang², Byungha Shin⁷, Jordi Arbiol^{8,13} , Huigao Duan¹⁴ , Yonghua Du^{15,16} , Marc Heggen¹⁷, Rafal E. Dunin-Borkowski¹⁷, Wanlin Guo⁵, Qi Jie Wang^{3,18}  , Zhuhua Zhang⁵   and Zheng Liu^{2,3,18,19}  

Rational design of noble metal catalysts with the potential to leverage efficiency is vital for industrial applications. Such an ultimate atom-utilization efficiency can be achieved when all noble metal atoms exclusively contribute to catalysis. Here, we demonstrate the fabrication of a wafer-size amorphous PtSe_x film on a SiO₂ substrate via a low-temperature amorphization strategy, which offers single-atom-layer Pt catalysts with high atom-utilization efficiency (~26 wt%). This amorphous PtSe_x (1.2 < x < 1.3) behaves as a fully activated surface, accessible to catalytic reactions, and features a nearly 100% current density relative to a pure Pt surface and reliable production of sustained high-flux hydrogen over a 2 inch wafer as a proof-of-concept. Furthermore, an electrolyser is demonstrated to generate a high current density of 1,000 mA cm⁻². Such an amorphization strategy is potentially extendable to other noble metals, including the Pd, Ir, Os, Rh and Ru elements, demonstrating the universality of single-atom-layer catalysts.

The high cost of noble metal sources, such as platinum and palladium, has hindered the broad deployment of fuel cells and metal–air batteries for commercial applications towards the development of sustainable energy^{1–3}. Taking the automotive system market as an example, the usage of the total Pt content in fuel cells was about 0.117 g kW_{gross}⁻¹ (kW_{gross} is the gross power of the fuel cell) in 2018, and it will be down to 0.108 g/kW_{gross}⁻¹ in 2020 and as low as 0.064 g kW_{gross}⁻¹ in 2025 for the cost demand in fuel cell systems⁴. To reduce the cost, nanostructuring a noble metal in various dimensions presents a promising strategy to improve utilization efficiency and lower the mass loading as well (Supplementary Table 1)^{5,6}. Currently, noble metals have been engineered into three-dimensional porous structures^{7,8}, two-dimensional (2D) nanosheets^{9,10}, one-dimensional nanowires^{11,12}, zero-dimensional clusters¹³ (Fig. 1a) or even items as

small as individual atoms^{14–16} (Fig. 1b). Such a trend will evolve into an ultimate landscape of noble metal atoms at the monolayer limit (for thickness ~1 nm), that is, single-atom-layer catalysis (Fig. 1c), wherein nearly all the atoms are reconfigurable for a maximum density while being accessible to catalytic reactions, capable of electrocatalytic activities and stable thermodynamically.

In this work, we demonstrate the synthesis of single-atom-layer Pt catalysis, using as an example atom-thin amorphous PtSe_x as a hydrogen evolution reaction (HER) electrocatalyst, and its potential to increase Pt utilization (Fig. 1c). First, we report the synthesis of a wafer-scale, one-nanometre-thick PtSe_x layer with amorphous yet robust structures through ion etching of predeposited 2D PtSe₂ under a low-density Ar plasma at a temperature of –30 °C. The loss of selenium atoms in the amorphous layer yields

¹State Key Laboratory of Chemo/Biosensing and Chemometrics, College of Chemistry and Chemical Engineering, Hunan University, Changsha, China.

²School of Materials Science and Engineering, Nanyang Technological University, Singapore, Singapore. ³Center for Opto-Electronics and Biophotonics, School of Electrical and Electronic Engineering & The Photonics Institute, Nanyang Technological University, Singapore, Singapore. ⁴Department of Physics, School of Physical and Mathematical Sciences, Nanjing Tech University, Nanjing, China. ⁵State Key Laboratory of Mechanics and Control of Mechanical Structures, Key Laboratory for Intelligent Nano Materials and Devices of Ministry of Education, and Institute for Frontier Science, Nanjing University of Aeronautics and Astronautics, Nanjing, China. ⁶SEU-FEI Nano-Pico Center, Key Lab of MEMS of Ministry of Education, School of Electronic Science and Engineering, Southeast University, Nanjing, China. ⁷Department of Materials Science and Engineering, Korea Advanced Institute of Science and Technology, Daejeon, Republic of Korea. ⁸Catalan Institute of Nanoscience and Nanotechnology (ICN2), Spanish National Research Council (CSIC), Barcelona Institute of Science and Technology (BIST), Barcelona, Spain. ⁹Institute of Flexible Electronics (IFE), Northwestern Polytechnical University, Xi'an, China. ¹⁰State Key Laboratory of Optoelectronic Materials and Technologies, School of Materials Science and Engineering, Sun Yat-sen University, Guangzhou, China. ¹¹NUS Graduate School, National University of Singapore, Singapore, Singapore. ¹²School of Physics and Electronics, Hunan University, Changsha, China. ¹³Institució Catalana de Recerca i Estudis Avançats (ICREA), Barcelona, Spain. ¹⁴College of Mechanical and Vehicle Engineering, Hunan University, Changsha, China. ¹⁵Institute of Chemical and Engineering Sciences, Agency for Science, Technology and Research, Singapore, Singapore. ¹⁶National Synchrotron Light Source II, Brookhaven National Laboratory, Upton, NY, USA. ¹⁷Ernst Ruska-Centre for Microscopy and Spectroscopy with Electrons, Peter Grünberg Institute, Forschungszentrum Jülich, Jülich, Germany. ¹⁸CNRS-International-NTU-Thales Research Alliance (CINTRA), Singapore, Singapore. ¹⁹Environmental Chemistry and Materials Centre, Nanyang Environment and Water Research Institute, Nanyang Technological University, Singapore, Singapore. ²⁰These authors contributed equally: Yongmin He, Liren Liu, Chao Zhu, Shasha Guo. ✉e-mail: ymhe@hnu.edu.cn; qjwang@ntu.edu.sg; chuwazhang@nuaa.edu.cn; z.liu@ntu.edu.sg

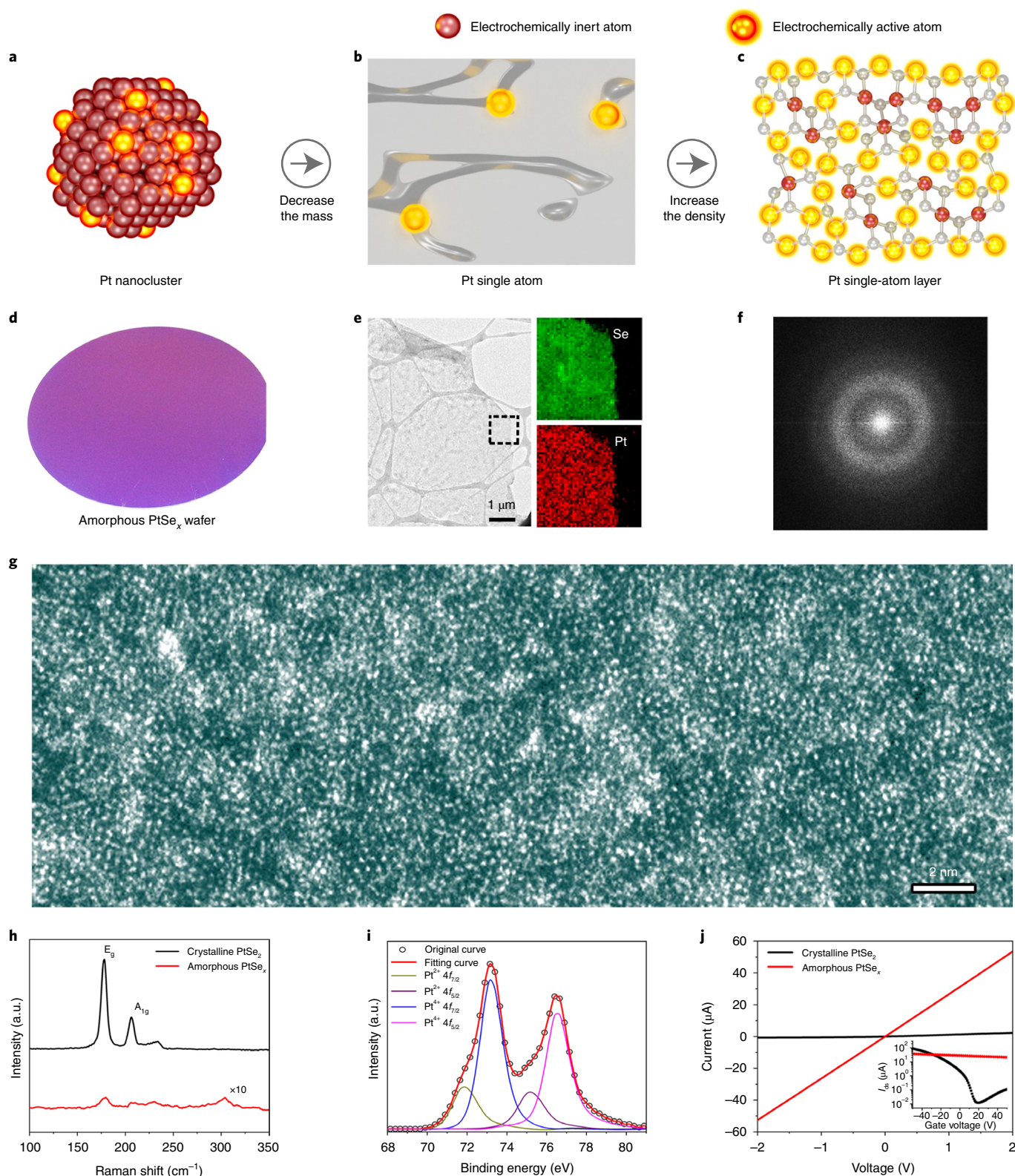


Fig. 1 | Pt single-atom-layer catalysis exemplified by an amorphous PtSe_x layer. **a–c**, Possible structural evolution of Pt catalysts from nanocluster (**a**) to single atom (**b**) and finally to single-atom layer with high-density active atoms (**c**). **d**, Photograph of a 2 inch wafer of amorphous PtSe_x film with ~ 1 nm thickness. **e**, TEM image of a suspended PtSe_x amorphous film, showing its uniform, continuous and atomically thin structure. EDX mapping images of Pt and Se in the selected dash box are shown on the right. **f, g**, Atomic-resolution aberration-corrected HAADF STEM image of an amorphous PtSe_x film in a large region (**g**) and the typical fast Fourier transform spectrum (**f**), showing a $>90\%$ ratio of amorphous regions in the whole film. **h**, Raman spectra of the amorphous film and 1T phase of the PtSe_2 crystal. **i**, Pt 4f XPS spectra of the amorphous film with fitted curves, showing no noticeable Pt(O) peaks. **j**, Current-voltage (I - V) curves of amorphous PtSe_x and few-layer crystalline PtSe_2 . Inset: the plot of the source-drain current (I_{ds}) as a function of gate voltage (back-gate field-effect transistor measurement), indicating the metallic property of the amorphous PtSe_x .

a stable Pt single-atom-layer phase on its surface, as evidenced by complementary characterizations, including atomic-resolution aberration-corrected high-angle annular dark-field (HAADF) scanning transmission electron microscopy (STEM), Raman spectroscopy, X-ray photoelectron spectroscopy (XPS) and X-ray absorption spectroscopy (XAS), and electrical measurements, and supported by intensive first-principles calculations. Next, our micro-electrochemical cell measurement shows that the amorphous PtSe_x layer exhibits excellent catalytic performance, similar to that of a pure Pt surface, with an onset potential of 0 V versus a reversible hydrogen electrode (RHE), Tafel slope of 39 mV dec⁻¹ and current density of 25 mA cm⁻² at a low potential of 50 mV versus RHE. The utility of the wafer-scale amorphous PtSe_x layer is further demonstrated in a water electrolyser, showing sustainable production of hydrogen. These results show a way to optimize the catalytic performance of 2D and similar materials based on amorphization.

Results

Fabrication of atomically thin amorphous film. We used low-temperature deep reactive ion etching (DRIE) with a low-density argon (Ar) plasma to convert the atomically thin crystalline PtSe₂ (1T phase) film into an amorphous PtSe_x film. First, a wafer-size (2 inch) PtSe₂ film was prepared through a two-step selenylation of Pt metal (~0.6 nm thickness) on a SiO₂/Si substrate, as explained in Supplementary Fig. 1. Then, the as-grown film was etched by DRIE at a low temperature of -30 °C for 50 seconds to obtain the amorphous PtSe_x layer (1.2 < x < 1.3). Figure 1d shows an ~1-nm-thick and wafer-scale PtSe_x film on a SiO₂/Si substrate (Supplementary Fig. 2). With a wet transfer method (as reported in Supplementary Fig. 3), a uniform and continuous film was suspended on a Cu-supported lacey carbon transmission electron microscopy (TEM) grid, as shown in Fig. 1e.

In order to characterize the synthesized PtSe_x, we conducted atomic-resolution HAADF imaging via STEM (Fig. 1f,g and Supplementary Figs. 4 and 5). The dark-field images of the PtSe_x film show a random distribution of the Pt atoms (bright spots in the image) in the film (Fig. 1g). Interestingly, there is no long-range order in the atomic arrangement, indicating that the achieved film is amorphous. Moreover, the typical fast Fourier transform spectrum (20 × 20 nm² area) has a broad and continuous halo (Fig. 1f) with no diffraction spots, which better visualizes a complete amorphization at an area up to nearly 4,000 nm² (Supplementary Fig. 4). Next, we randomly chose five regions in the PtSe_x film whose STEM images showed a uniform amorphization process over a large scale (Supplementary Fig. 5). This amorphization process is also verified by Raman spectra, which exhibit nearly negligible characteristic peaks (E_g and A_{1g}) compared to the crystalline PtSe₂ film (Fig. 1h). In contrast with previously reported amorphous carbon monolayers¹⁷ (0.6 nm thickness), our amorphous PtSe_x layer is made of Pt and Se atoms with more complicated coordination and, to the best of our knowledge, is the first binary amorphous layer. Notably, our amorphous layer can be thermodynamically stable in a 2D form with a thickness down to 1 nm. Such a highly stable, ultrathin amorphous layer has been long sought, since it can expose nearly all the Pt atoms to electrocatalysis, as will be discussed later.

The formation of the amorphous layer is largely attributed to the low-temperature processing and the low-density Ar plasma. The low-temperature selenylation of Pt films avoids the solid-state dewetting behaviour¹⁸ that forms a porous film (Supplementary Fig. 6), and the low-temperature substrate (approximately -30 °C, during DRIE) suppresses the plasma-induced local heating that may cause aggregation of surface atoms and lead to incomplete amorphization (Supplementary Fig. 7). The low-density Ar plasma¹⁹ drives the phase transition of PtSe_x smoothly by adjusting the etching duration. During the DRIE process, the original film evolves from a crystalline 1T phase (PtSe₂), via a defected 1T phase and then a

mixture of amorphous structure and 1T phase (PtSe_{1.3<x<1.4}), finally to a completely amorphous structure (PtSe_{1.2<x<1.3}), as shown in Supplementary Fig. 8.

We further performed XPS and XAS measurements to probe the local electronic structure of Pt atoms in the amorphous PtSe_x. The XPS measurement shows both Pt(IV) and Pt(II) present in the Pt 4f region, while no significant Pt(0) peaks are found (Fig. 1i and Supplementary Figs. 9 and 10). These XPS data at Pt 4f indicate that the amorphous PtSe_x is a Pt–Se compound but not isolated Pt and Se nanoparticles, consistent with our STEM observations. In the XAS measurement, no pronounced Pt–Pt bond peak was found in amorphous PtSe_x, confirming that there are no isolated Pt nanoparticles (Supplementary Fig. 11). Compared with crystalline PtSe₂, a lower Pt–Se coordination number in PtSe_x (coordination number: 5.1) and an elongated bond length (~0.02 Å) were observed in XAS data, indicating that the structural homogeneity is reduced in the amorphous structure. Finally, the back-gate electrical measurements (Fig. 1j) show that the amorphous PtSe_x exhibits a high conductance (a resistivity of ~0.03 Ω mm) and no gating effect (inset of Fig. 1j), in contrast to a p-type semiconducting behaviour of crystalline PtSe₂. This result suggests an amorphization-induced metalization of the PtSe_x layer.

Formation mechanism of the amorphous film. We then performed ab initio calculations to understand the formation mechanism of amorphous PtSe_x (Methods). To mimic the loss of Se atoms that is induced by ion etching, Se atoms were removed sequentially from a perfect single-crystal PtSe₂, while ensuring that the removed atom at each step was the one that costs the minimum energy. Note that we cannot simulate a real amorphous structure but aim to shed light on the local structural evolution induced by DRIE. To quantify the structural-deformation degree of PtSe_x induced by the Se removal, we define a parameter based on the displacement of Pt atoms, δ_{pt} , expressed by $\delta_{pt} = |P_i - P_i^0|$ with $i = 1, 2, \dots, N$, where N is the total number of Pt atoms in the supercell, and P_i and P_i^0 are the positions of i th Pt atom in the PtSe_x and perfect single-crystal PtSe₂, respectively. Then, an averaged displacement of Pt is given by $\langle \delta_{pt} \rangle = \sum |P_i - P_i^0| / N$. The sequential Se removal yields a distinct vacancy order in the film, in which each Se vacancy connects to neighbouring vacancies with four-coordinated Pt atoms (Fig. 2a). However, the 1T framework of defective PtSe_x is barely distorted even when x decreases to 1.5, as supported by the calculated δ_{pt} and $\langle \delta_{pt} \rangle$ values shown in Fig. 2a. These results suggest that the crystalline structure of PtSe_x (that is, 1.5 < x < 2) is rather robust to short-term ion etching, in line with our experimental results.

Further decreasing the ratio of Se ($x < 1.5$) leads to three-coordinated Pt atoms. Every two of these three-coordinated Pt atoms resulting from the same Se removal shift towards each other to stabilize the 2D PtSe_x (green circles in atomic structures in Fig. 2a), then severely disturbing the local bond networks. However, the overall structure remains essentially crystalline if the three-coordinated Pt atoms are insufficiently dense (Fig. 2a). In our calculations, both relaxed structures and calculated $\langle \delta_{pt} \rangle$ values suggest that the local amorphization starts at a Se/Pt ratio of ~1.38, and a complete amorphization occurs at a ratio of 1.33 with $\langle \delta_{pt} \rangle$ exceeding 1.0 Å (Fig. 2a,b, Supplementary Figs. 12–18 and Source Data). The amorphization is rooted in the randomness of creating three-coordinated Pt atoms across the whole layer. For the amorphous PtSe_{1.33}, we already cannot find long-range lattice order within our supercell. The general trend of amorphization agrees with our experimental observation (Supplementary Fig. 8). Further decreasing x in 2D PtSe_x enhances the amorphous character, as evidenced by the relaxed structures of PtSe_{1.33}, PtSe_{1.30}, PtSe_{1.27} and PtSe_{1.25} (Fig. 2a,b).

Experimentally, the detailed amorphous structure is analysed by mapping the precise position of Pt atoms in PtSe_x based on

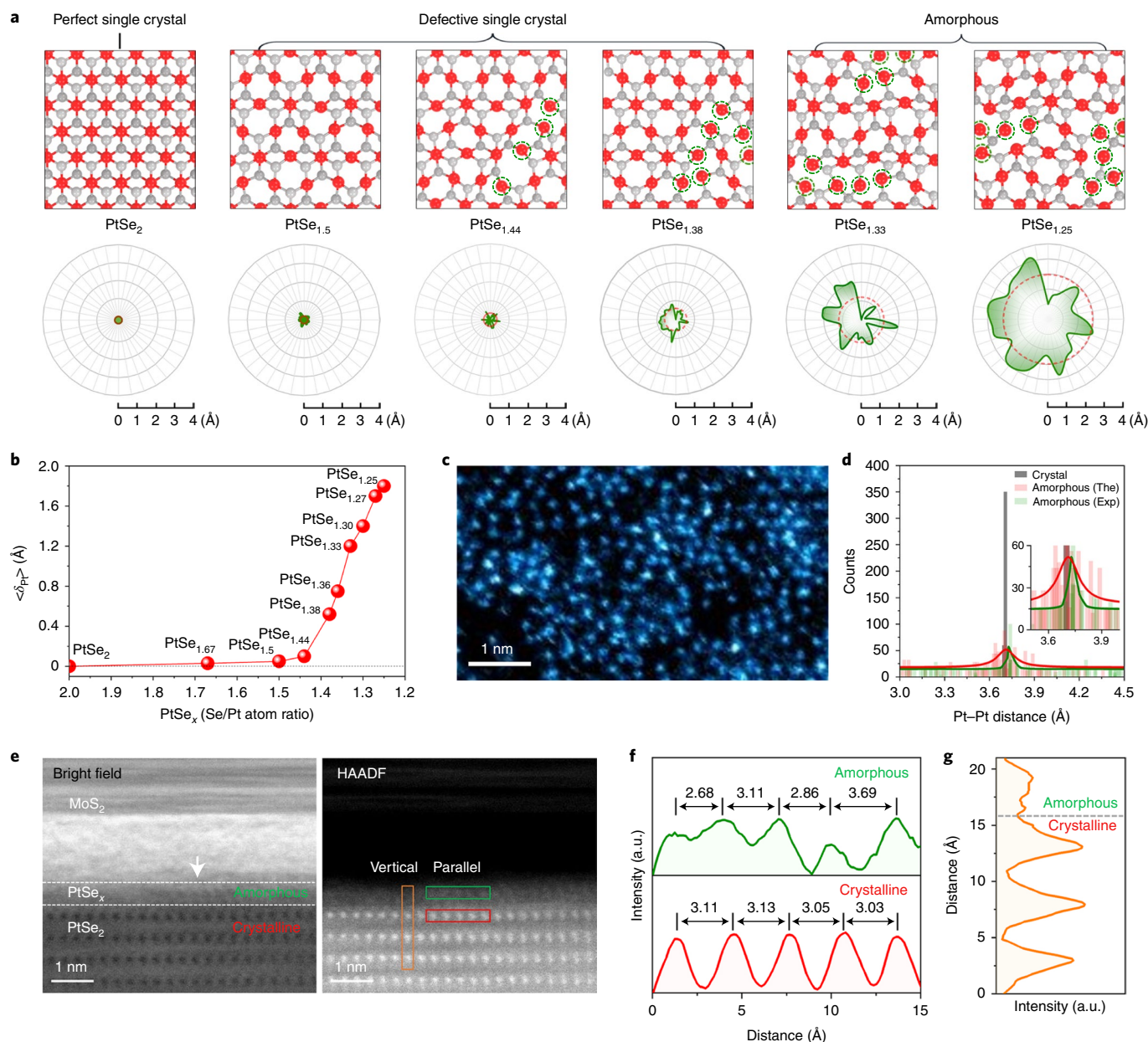


Fig. 2 | Formation mechanism of the 2D amorphous PtSe_x . **a**, AIMD simulations for the structural evolution of PtSe_x with decreasing x (Pt atom in red, Se atom in grey). In atomic structures, undercoordinated Pt atoms are marked by green dashed circles. Green lines and shading in the lower figures show the displacement δ_{Pt} of 36 Pt atoms (denoted by 36 radial grey lines) from their ideal positions in a PtSe_2 supercell, while the red dashed lines give the averaged displacement of all Pt atoms in PtSe_x , that is, $\langle \delta_{\text{Pt}} \rangle$. The atomic coordinates of the optimized models are provided in the Source Data. **b**, Theoretical calculation of $\langle \delta_{\text{Pt}} \rangle$ in the 2D PtSe_x as a function of x . An amorphous characteristic can be observed when x decreases to 1.38. **c**, Experimental investigation of the distribution of Pt atoms in an amorphous PtSe_x in false-coloured atomic-resolution aberration-corrected HAADF STEM. **d**, Statistical distributions of the distance between two adjacent Pt-Pt atoms in amorphous PtSe_x and crystalline PtSe_2 monolayers from both experiment (Exp) and theoretical (The) results. The red curve was collected from the experimental results and the green one from the theoretical calculation. The inset shows a zoomed-in view. **e**, Bright-field and HAADF STEM images of the cross-sectional structure of an amorphous PtSe_x layer. **f**, Parallel intensity profiles of the amorphous PtSe_x layer and crystalline PtSe_2 layer, according to the green and red squares in the HAADF image, respectively. **g**, Vertical intensity profile of the atom columns across amorphous PtSe_x and crystalline PtSe_2 layers, according to the orange square in the HAADF image.

our STEM imaging (Fig. 2c), which allowed us to determine the projected distances between two adjacent Pt atoms, projected onto the basal plane. The data for a perfect PtSe_2 sheet are taken as a reference. It turns out that the projected Pt-Pt distances in the amorphous $\text{PtSe}_{1.33}$ peak at an ideal 3.73 Å but exhibit a much broader distribution over 3.0–4.5 Å than those in perfect PtSe_2 (Fig. 2d and Supplementary Fig. 19). These distances agree well

with our ab initio molecular dynamical calculations regarding the broad distribution and the peak position (Fig. 2d), as do the Pt-Se bond angles in the 2D PtSe_x (Supplementary Fig. 20). Such a broad distribution of the bond geometry also echoes the results in the reported amorphous carbon monolayers¹⁷ and O-Si-O bonds in a silica bilayer²⁰, featuring a 2D amorphous network without long-range order.

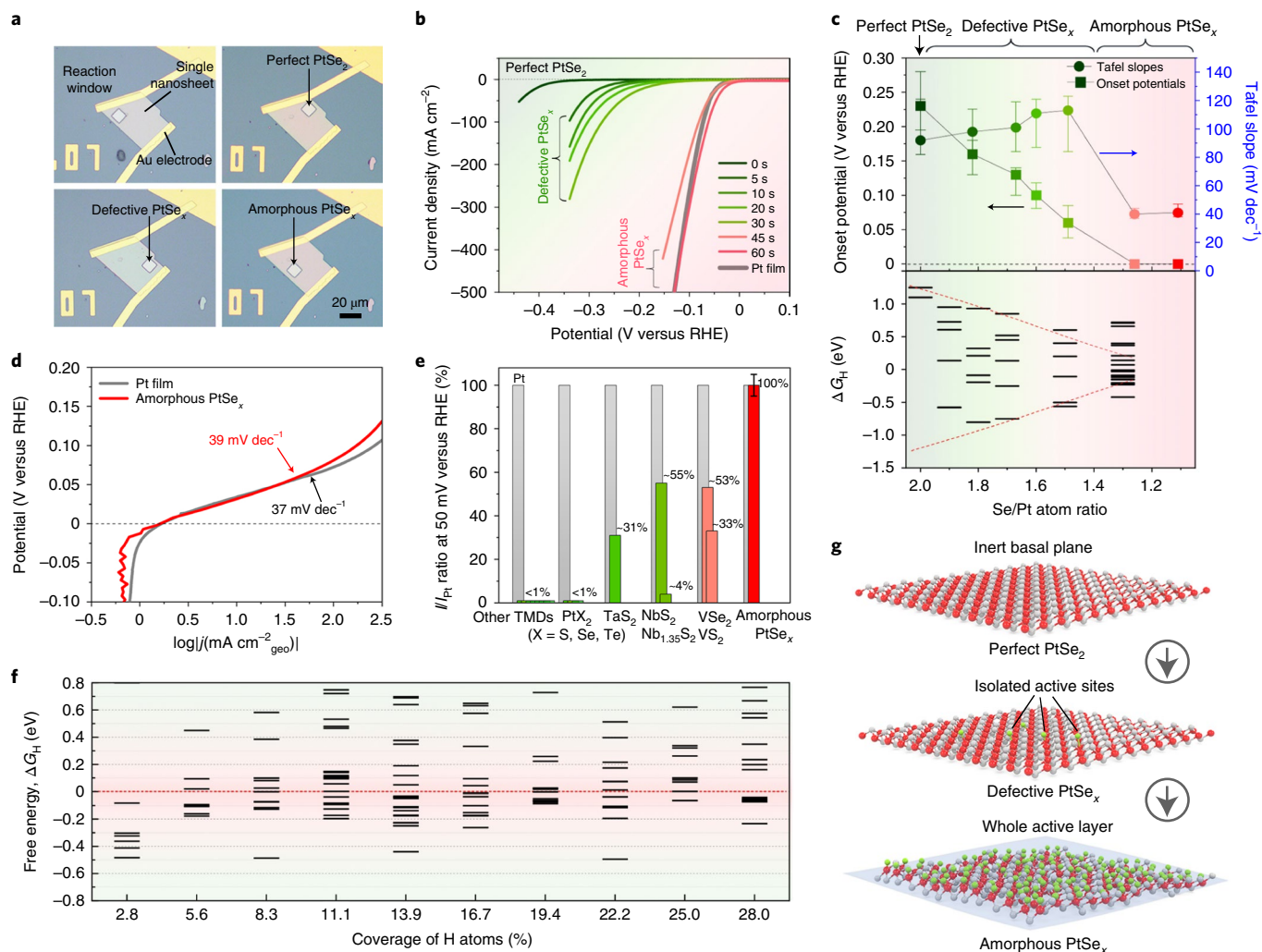


Fig. 3 | HER activity of amorphous PtSe_x catalyst by a micro-electrochemical cell. **a**, Optical images of PtSe_x microelectrodes with reaction windows, showing four typical reaction windows with different plasma treatment times on a single nanosheet, where spatial control of the electrocatalytic reaction was achieved in different regions by carving windows on a passive PMMA layer. **b**, Polarization curves of the PtSe_x nanosheet with a treatment duration from 0 to 60 s, corresponding to x varying from 2.0 to 1.11. **c**, Transition of HER catalytic sites of PtSe_x as a function of x . In the experimental results (top), the onset potentials and Tafel slopes were measured on tens of devices, showing the near inertness (electrochemically) of perfect single-crystal PtSe_2 , the moderate activity of defective single-crystal PtSe_x ($1.5 < x < 2$) and the high activity of amorphous PtSe_x ($x \leq 1.4$) with a nearly zero onset potential and a 40 mV dec^{-1} Tafel slope; the error bars represent the range of values for those independent devices. The theoretical calculations (bottom) provide the Gibbs free energy (ΔG_{H}) of PtSe_x with different x from the calculation, where the red dashed lines show the trend of ΔG_{H} . **d**, Comparison of the Tafel slopes between amorphous PtSe_x and Pt film. **e**, Current density ratios of TMD-based catalysts with respect to the Pt catalyst at 50 mV versus RHE. The amorphous PtSe_x shows -100% current density ratio, and the error bars represent the range of its values in our experiment. The data of other TMD-based catalysts and their corresponding Pt catalysts were collected from the literature. **f**, Calculated Gibbs free energy (ΔG_{H}) for hydrogen adsorption on an amorphous $\text{PtSe}_{1.33}$ with the coverage varying from 2.8% to 28%. **g**, Schematic of isomer structures of H atoms adsorbed on the amorphous PtSe_x surface, demonstrating the amorphous $\text{PtSe}_{1.33}$ acting as a single-atom-layer catalyst as a whole. The perfect PtSe_2 (inert basal plane) and defective PtSe_x (scattered Se vacancies as active sites) are shown for comparison.

We also carried out cross-sectional STEM to investigate the amorphous monolayer's structure (details in Methods). Figure 2e shows the bright-field and HAADF STEM images of the cross-sectional structure, exhibiting the amorphization of the surface PtSe_x monolayer (highlighted by the white dashed lines), in sharp contrast to the very crystalline PtSe_2 underlayers. The parallel intensity profiles (Fig. 2f) show that the amorphous PtSe_x monolayer possesses inconsistency in both the intensity distribution and interatomic distance, indicating an obvious in-plane displacement of Pt atoms compared to the periodic profile of the crystalline PtSe_2 monolayer. The vertical intensity profiles (Fig. 2g) exhibit a reduced intensity and broadened peak of an amorphous PtSe_x monolayer,

verifying an out-of-plane displacement of Pt atoms. These results suggest that the Pt displacement can occur in any direction but is strictly restricted within a single layer, forming an amorphous PtSe_x monolayer structure.

Catalytic activity of amorphous film. The HER activity of the amorphous PtSe_x is tested using micro-electrochemical cells^{21,22}, as shown in Fig. 3a and Supplementary Figs. 21 and 22. Starting from the same mechanically exfoliated PtSe_2 nanosheet, we etched different regions at controlled duration and obtained regions of perfect single-crystal, defective single-crystal and amorphous PtSe_x for a fair comparison among their HER activities. Note that this

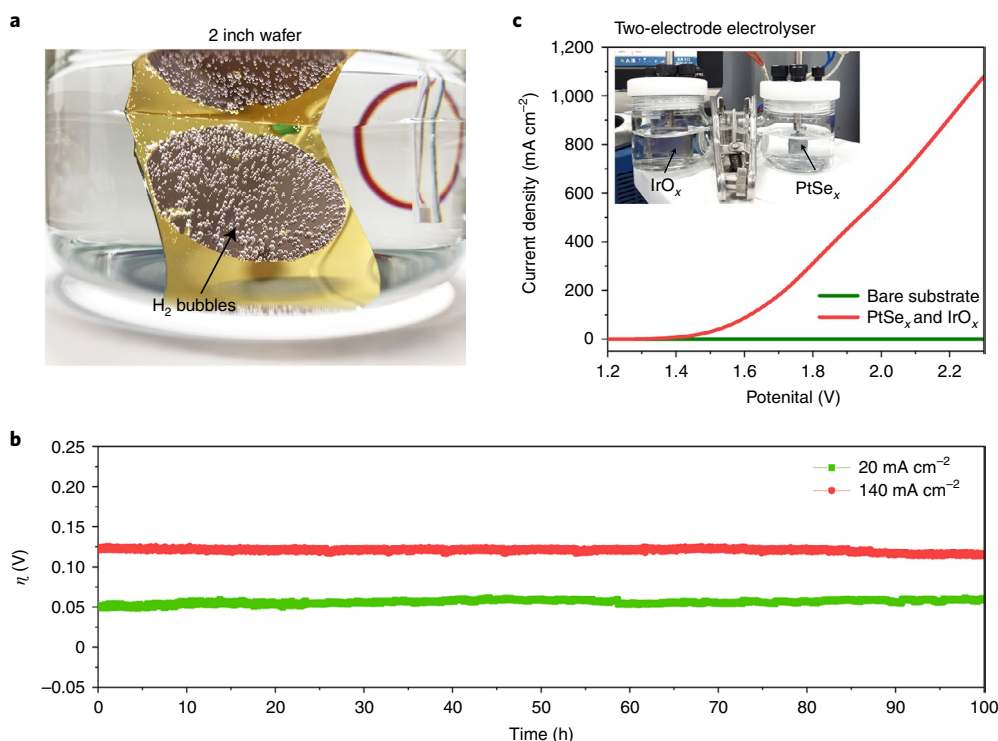


Fig. 4 | Wafer-scale fabrication and stability of amorphous PtSe_x catalyst. **a**, A 2 inch amorphous PtSe_x film fabricated on a $\text{Au}/\text{SiO}_2/\text{Si}$ substrate for mass production of hydrogen gas. **b**, Time-dependent overpotential (η) curves under different current densities ($j = 20 \text{ mA cm}^{-2}$ and 140 mA cm^{-2}) in $0.5 \text{ M H}_2\text{SO}_4$ aqueous solution. **c**, I - V curves of overall water splitting in the two-electrode electrolyser, made of an IrO_x anode and a PtSe_x cathode. Inset: the photograph of a two-electrode electrolyser cell.

cell structure can exclude the possible influence from the underlying PtSe_2 (Supplementary Figs. 23 and 24). The electrocatalytic performances of these regions are summarized in Fig. 3b and Supplementary Fig. 25. First, the basal plane of the perfect single crystal is HER-inert, as has been widely measured^{19,23}. Second, at the initial stage of the plasma etching, only isolated Se vacancies are created as active sites, yielding a moderate HER performance (onset potential, $\sim 0.1 \text{ V}$ versus RHE; Tafel slope, $\sim 100 \text{ mV dec}^{-1}$). An increased number of Se vacancies results in an enhanced HER performance. Third, as the treatment continues, amorphous PtSe_x is formed and exhibits excellent catalytic performance, for example, an onset potential of 0 V versus RHE, Tafel slope of 39 mV dec^{-1} and current density of 25 mA cm^{-2} at 50 mV versus RHE for the $\text{PtSe}_{1.26}$. A sharply improved performance is observed during this process due to the transition of the catalytic site, that is, from Se vacancies to the amorphous Pt sites.

We next tested tens of micro-devices and combined the calculation of the Gibbs free energy of adsorbed hydrogen atoms (ΔG_{H}) on perfect single-crystal, defective single-crystal and amorphous PtSe_x to investigate in detail the transition of active sites (Fig. 3c and Supplementary Fig. 26). For a pristine crystalline PtSe_2 , the calculated ΔG_{H} for inequivalent sites is higher than 1 eV (Fig. 3c), indicating their poor catalytic activity, which agrees with our experiments. When Se vacancies are introduced in the PtSe_x monolayer, the spectrum of ΔG_{H} is broadened, and an overall trend is that the values of ΔG_{H} get closer to zero with increasing the vacancy density (x decreases from 1.8 to 1.5; Fig. 3c). This is in line with our experimental results, which show that the catalytic performance is enhanced with decreasing x . Significant change arises when the PtSe_x monolayer is amorphized upon further decreasing x to 1.4. In this case, active sites are remarkably propagated, as evidenced by the crowding of ΔG_{H} near 0 eV , due to the

existence of the three-coordinated Pt structure. This result also agrees with the measured, superior catalytic performance of the amorphized $\text{PtSe}_{1.26}$.

It is compelling to see that the amorphous PtSe_x offers a comparable catalytic performance to pure Pt, which is seen by the onset potential of 0 V versus RHE, Tafel slope of 37 mV dec^{-1} and current density of 25 mA cm^{-2} at 50 mV versus RHE (Fig. 3b,d). The Tafel curves in Fig. 3d reveal a similar rate-limiting step for the reaction kinetics between the amorphous PtSe_x and pure Pt (ref. 24), rendering the amorphous PtSe_x with a Pt-like catalytic characteristic. More importantly, the nearly 100% current density indicates a maximal density of active sites enabled by the amorphous structure (Fig. 3e). This ratio, to the best of our knowledge, is a record high among current transition metal dichalcogenide (TMD) catalysts, especially in light of the fact that the current density is less than 1% in PtX_2 ($X = \text{S}, \text{Se}, \text{Te}$) and other TMDs and ranged between 4% and 55% in metallic VS_2 , VSe_2 , NbS_2 , $\text{Nb}_{1.35}\text{S}_2$ and TaS_2 catalysts (Supplementary Fig. 27 and Supplementary Table 2 for comparison).

To gain further insight into the electrocatalytic performance of amorphous PtSe_x , we take the hydrogen coverage into account to evaluate the catalytic activity of the whole layer. This is because the amorphous PtSe_x layer may provide a layer of Pt sites with different reactivities. The hydrogen coverage^{25,26} is defined as $\theta = \frac{N_{\text{H}}}{M_{\text{Pt}}}$, where N_{H} is the number of hydrogen atoms and M_{Pt} is the total number of Pt sites (Supplementary Figs. 28–37). The hydrogen coverage varies from 2.8% to 27.8% (Supplementary Note 1). Unlike Pt in single-atom catalysts (for example, Pt-doped in TMDs²⁷ and graphene¹⁵), the Pt atoms with diverse bond geometries in the amorphous PtSe_x yield a wide range of ΔG_{H} as shown in Fig. 3f. If we consider that the Gibbs free energy ΔG_{H} (eV) of the active sites falls in the range of $(-0.2, 0.2)$ (Supplementary Note 2 and Supplementary Fig. 38), then $\sim 25 \text{ wt\%}$ Pt atoms could contribute

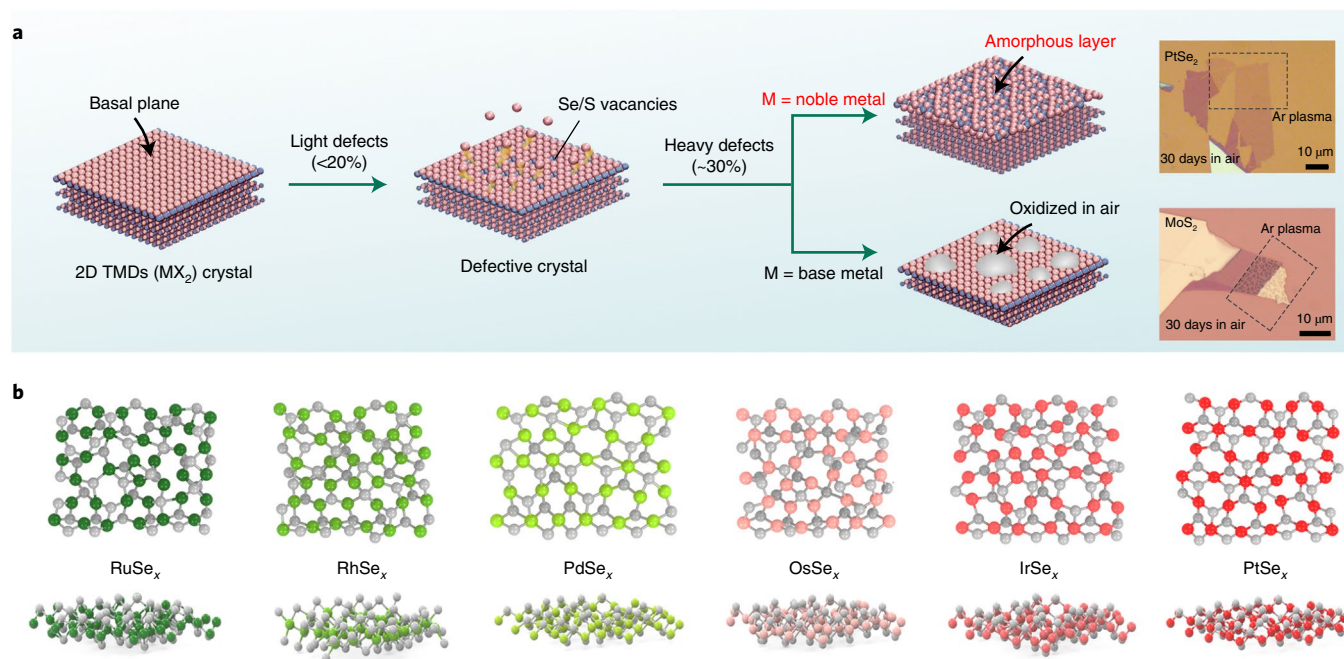


Fig. 5 | Possible amorphous structures in other noble metal selenides. **a**, Schematic of structural evolution of perfect single-crystal TMDs, showing that the amorphous structures of noble-metal-based MX_x ($M = \text{Pt}, \text{Pd}, \text{Ir}, \text{Os}, \text{Ru}, \text{Rh}$) are possibly stable in air due to resistance to corrosion and oxidation, in contrast to base-metal-based MX_x ($M = \text{Mo}, \text{W}, \text{Re}$ and so on) with overexposed M atoms readily oxidized in $\text{O}_2/\text{H}_2\text{O}$ atmosphere. The optical images show distinct morphologies of MoS_2 and PtSe_x in air for 30 days after Ar-plasma treatment, where small droplets exist on plasma-treated regions of MoS_2 . **b**, Possible amorphous structures obtained from AIMD simulations for PtSe_x , PdSe_x , IrSe_x , OsSe_x , RuSe_x and RhSe_x (where $x = 1.33$; Se atom in grey). The atomic coordinates of the optimized models are provided in the Source Data.

to the HER at a hydrogen coverage of 28%. Such an unusual high density of active sites is attributed to the three-coordinated Pt atoms that not only enhance the density of states of $5d$ orbitals near the Fermi level but also provide a favourable coordination environment for catalysis (Supplementary Figs. 39 and 40). Based on the calculations, we tentatively estimate an atom-utilization efficiency of Pt atoms up to ~25 wt% in the amorphous PtSe_x . This value is very close to that obtained from our Cu-underpotential-deposition measurement (~26 wt%; Supplementary Fig. 41) and is much higher than the ~5 wt% in previously proposed single-atom Pt catalysts⁶. Such a high atom-utilization efficiency may explain why the amorphous PtSe_x can deliver a nearly 100% current density relative to the pure Pt metal. Thus, we name the amorphous PtSe_x as a single-atom-layer catalyst (Fig. 3g), a type of Pt catalyst comparable or even superior to the widely studied single-atom or other reported Pt catalysts (Supplementary Table 3).

Stability and large-scale hydrogen production of amorphous catalyst. As a proof-of-concept for hydrogen generation, the 2 inch amorphous PtSe_x layer is transferred onto a Au substrate for mass production of hydrogen. Figure 4a shows the large amount of hydrogen bubbles produced from this catalyst (also Supplementary Fig. 42 and Supplementary Video 1). We further examine the catalytic stability of amorphous PtSe_x . The chrono-potentiometric test (overpotential versus time) conducted for 100 hours shows that this amorphous PtSe_x also possesses long-term stability at both small and large current densities, that is, 20 and 140 mA cm^{-2} , respectively (Fig. 4b and Source Data). What is more, after the long-term testing, the material's morphology and structures are well retained, confirming the stable amorphous structure during the HER process (Supplementary Figs. 43 and 44).

We also made a two-electrode electrolyser cell for overall water splitting, as shown in Fig. 4c. The assembled full cell consists of an

amorphous PtSe_x layer on a fluorine-doped tin oxide (FTO) substrate as a cathode and an IrO_x film as an anode (inset of Fig. 4c and Supplementary Video 2). The reaction initially has a low onset potential of 1.25 V, close to the theoretical voltage limit (1.23 V). Meanwhile, the current density of this electrolyser is as high as 250 mA cm^{-2} at 1.7 V, and later reaches up to $1,000 \text{ mA cm}^{-2}$. These parameters are superior to those reported for electrolysers based on thin 2D materials with a current density of $10\text{--}100 \text{ mA cm}^{-2}$ at similar reaction potentials²⁸, and are even close to those of industrial Pt and Ir electrolysers ($\sim 1,000 \text{ mA cm}^{-2}$)^{29,30}. In real applications, the loss or deactivation of noble metal catalysts remains a major issue. To address this issue, we developed a layer-by-layer replenishment method of amorphous PtSe_x using a controlled etching (Supplementary Figs. 45 and 46). Once the old amorphous PtSe_x layer becomes catalytically inactive, a new amorphous layer will be created. Such a process persists at least to the sixth new layer without obvious decay in current densities and Tafel slopes, suggesting a successful replenishment.

Figure 5a presents a general approach to achieve amorphous noble MX_x libraries ($M = \text{Pt}, \text{Pd}, \text{Ir}, \text{Os}, \text{Ru}, \text{Rh}$; $X = \text{S}, \text{Se}$) via defect engineering. As the defect concentration increases, the original lattice structure is increasingly distorted. The as-produced amorphous MX_x would be stable in air due to the inert nature of noble metals, as demonstrated by PtSe_x in our work. Indeed, our high-throughput ab initio molecular dynamics (AIMD) calculations suggest that all other noble metal selenide layers, such as PdSe_x , IrSe_x , OsSe_x , RuSe_x and RhSe_x , form stable amorphous layers as well (Fig. 5b, Source Data and Supplementary Fig. 47). Notably, our preliminary experiments have realized a stable amorphous PdSe_x layer (Supplementary Figs. 48 and 49). By contrast, most MX_x based on non-noble metals ($\text{Mo}, \text{W}, \text{Re}$ and so on) are unstable or even decompose in air due to the corrosion and oxidation of exposed metal atoms (MoS_2 as an example in Fig. 5a and Supplementary Fig. 50).

Conclusions

We have demonstrated a highly stable amorphous layer of noble metal chalcogenides—as exemplified by amorphous PtSe_x—by Ar-plasma etching of pristine noble metal dichalcogenides at low temperatures, and we have disclosed the transition mechanism of amorphous PtSe_x from perfect PtSe₂. This amorphous PtSe_x layer of ~1 nm thickness provides a robust single layer of noble metal atoms that exhibits an electrocatalytic performance rivalling that of pure noble metals, along with a high atom-utilization efficiency. A two-electrode electrolyser cell made of PtSe_x as cathode and IrO_x as anode has delivered a promising overall water splitting performance compared to existing 2D-materials-based devices. Beyond the PtSe_x material, our work also opens opportunities to design a family of noble metal single-atom-layer catalysts from their amorphous selenides, such as PdSe_x, IrSe_x, OsSe_x, RuSe_x and RhSe_x, greatly boosting the potential for various electrocatalytic applications.

Methods

Fabrication of wafer-size PtSe_x film. There are three steps involved in the fabrication process. The first is depositing ~0.6-nm-thick Pt layers on a clean 2 inch sapphire or SiO₂/Si wafer by electron-beam evaporation at the rate of 0.1 Å s⁻¹. The deposition temperature of the substrate is kept at room temperature to avoid the agglomeration of the film. The second step is selenizing those metal films in a chemical vapour deposition apparatus, which is depicted in detail in Supplementary Fig. 1. Selenium powder is loaded in an aluminium oxide boat and placed at both the upstream and middle of the tube, enabling a continuous supply of selenium vapour sources. The selenylation temperature was first kept at 200 °C in low-vacuum conditions of 10–100 kPa for 1–2 hours. This low temperature will avoid the solid-state dewetting behaviour¹⁸ that forms a porous film (Supplementary Fig. 6). Later, the temperature was increased to 550 °C to realize complete selenylation. Third, the samples were exposed to an Ar-plasma atmosphere at a low temperature (approximately –30 °C) for various treatment durations. The low-density Ar plasma was generated by a DRIE system (Oxford PlasmaLab System 100) with a 5 W radio frequency (RF) power in a vacuum chamber (10⁻³ torr of plasma pressure). A low pressure promises a short mean free path for the radicals in a plasma atmosphere. A low-temperature (approximately –30 °C) substrate will hinder the plasma-induced local heating that usually causes the surface atoms' aggregation and leads to an uncompleted amorphization.

First-principles calculations. The calculations were performed within the density functional theory framework with the Perdew–Burke–Ernzerhof functional³¹, as implemented in the Vienna Ab initio Simulation Package code³². A vacuum space of 20 Å was set to eliminate spurious interaction between two PtSe_x surfaces in adjacent periodic images. The core electron–ion interaction was described by the projector augmented wave potential^{31,33}, and the cut-off energy of the plane-wave basis was set to be 450 eV. We simulated a bilayer PtSe₂ with a large 15 × 15 supercell, where the atoms in the bottom layer were fixed while those in the top layer were allowed to relax. The Brillouin zone integration was sampled using 4 × 4 × 1 *k* points for the structural optimization, 2 × 2 × 1 *k* points for AIMD simulations and 16 *k* points for electronic calculations. The atomic positions were optimized until the maximum force on each atom was less than 0.01 eV Å⁻¹. The NVT ensemble (the canonical ensemble, in which the amount of substance (*N*), volume (*V*) and temperature (*T*) are conserved) was used for AIMD simulations.

The structures of the PtSe₂ crystal with PtSe_x surface were obtained by sequentially removing Se atoms from the PtSe₂ monolayer. Since the simple structural optimization was run at 0 K and, thus, tends to reach a local minimum, we performed AIMD calculations for the Se-depleted PtSe_x monolayers to locate the amorphized structures. We raised the simulation temperature to 1,000 K to accelerate the structural relaxation for 8 ps. Then, each relaxed structure from the AIMD simulation was fully relaxed at 0 K. Finally, the thermal stability of all the optimized structures was reexamined by a 5 ps AIMD simulation at 800 K. Given the effect of the Ar plasma on the PtSe_x surface, the bond rotation in PtSe_x is considered to a certain extent. The atomic coordinates of the optimized models are provided in the Source Data.

Theoretical calculation of Δ*G*_H. The calculations of Δ*G*_H were also performed by using the Perdew–Burke–Ernzerhof generalized gradient approximation method. A kinetic energy cut-off was set to 500 eV for the plane-wave expansion in this set of calculations. The Gibbs free energies Δ*G*_H at 300 K were calculated as

$$\Delta G_{\text{H}} = \Delta E + \Delta E_{\text{ZPE}} - T\Delta S_{\text{H}}, \quad (1)$$

$$\Delta E = E_{\text{surf}+n\text{H}} - E_{\text{surf}+(n-1)\text{H}} - 1/2E_{\text{H}_2}, \quad n = 1, 2, 3, \quad (2)$$

$$\Delta E_{\text{ZPE}} - T\Delta S_{\text{H}} = 0.173 \text{ eV}, \quad (3)$$

where Δ*E* is the adsorption energy of the *n*th hydrogen atom on the system with respect to the gas phase, *T* is the temperature, Δ*S*_H is the entropy of a H atom adsorbed on the PtSe_x substrate, *E*_{surf+*n*H} is the energy of the PtSe_x substrate with *n* hydrogen atoms, *E*_{H₂} is the energy of a free H molecule and Δ*E*_{ZPE} is the zero-point vibrational energy. The harmonic approximation was employed for the vibrational analysis of adsorbates, while gas phase reference molecules were treated as ideal.

Fabrication of PtSe₂ nanosheet-based micro-device. First, 16 mm × 16 mm chips of SiO₂ (285 nm) on Si with 31 prepatterned Au contact pads were fabricated using photolithography. Second, mechanically exfoliated PtSe₂ nanosheets were transferred onto the chips. Third, metal electrodes were made on the nanosheet by electron-beam lithography followed by thermal or electron-beam evaporation of 5 nm/60 nm Cr/Au. Finally, the device chip was passivated with 500 nm poly(methylmethacrylate) (PMMA) film, followed by an electron-beam lithography process to create the window on the PMMA to expose the regions (*d*₁–*d*₃) of interest on the nanosheet. As the PMMA is inert in the potential range investigated, we expect the electrochemical reactions to occur only on the exposed regions. Note that we choose the mechanically exfoliated PtSe₂ nanosheet due to its perfect atomic surface, guaranteeing that no other activity sites (defects or edges) can interfere with the measurement. The thickness of the employed PtSe₂ nanosheet is about 21 nm. The reaction windows were opened at the desired regions on the same nanosheet with various Ar-plasma treatment times. As a result, this micro-cell method allows a rigorous (or even semi-quantitative) investigation of the surface evolution of PtSe₂ from the 1T phase to amorphous. Additionally, the thickness influence of underlying PtSe₂ on the HER performance was examined by thickness-dependent micro-devices (Supplementary Fig. 23) and in situ electronic/electrochemical measurements (Supplementary Fig. 24). A negligible effect was observed, indicating a reliable measurement in our cell.

Fabrication of 40-nm-thick Pt-film-based micro-device. To precisely compare the electrocatalytic performance between Pt and amorphous PtSe_{1.36}, we made a Pt microelectrode. A variety of Pt/Ti (40 nm/2 nm) nanostrips were fabricated onto the aforementioned prepatterned chip by a laser writing method followed by electron-beam evaporation of 2 nm Ti and 40 nm Pt. The bottom Ti layer employed here served as an adhesion layer between the Pt film and SiO₂/Si substrate. As with the previously mentioned micro-cell device, a reaction window was opened in the PMMA passivation film by electron-beam lithography to expose the Pt film for HER measurement.

Micro-electrochemical measurement. A micro-electrochemical measurement^{21,34} was employed in our work. Among the four electrodes, two were connected to graphite (high purity) and a Ag/AgCl micro reference electrode (Harvard Apparatus; calibration in Supplementary Fig. 22) to function as the counter and reference, respectively. The other two electrodes were connected to the PtSe_x nanosheets as drain and source contacts to collect their conductive and electrocatalytic signals during the HER process. In all experiments, only the exposed region of the nanosheets contributes to the electrocatalytic performance, and the rest of the area in contact with the electrolyte was passivated using PMMA film. During a micro-cell measurement, the scan rate of the electrochemical potential is 10 mV per step. The electrocatalytic current density was calculated by normalizing the current to the open area of PMMA on the nanosheets. In this work, we express the electrochemical reference voltage with respect to RHE, given by

$$E_{\text{RHE}} = E_{\text{Ag/AgCl}} + 0.219 \text{ V}. \quad (4)$$

The mass activity of Pt in our amorphous PtSe_{1.26} catalyst is evaluated using the following equation:

$$\text{Mass activity}_{\text{Pt}} = \frac{I}{m} = \frac{J (\text{mA cm}^{-2})}{66.2\% \times \rho (\text{mg cm}^{-3}) \times t (\text{cm})} = \frac{J}{0.313} (\text{A mg}_{\text{Pt}}^{-1}) \quad (5)$$

where *I* is the current, *m* is the mass of Pt, *J* is the current density, *ρ* is the density of PtSe_{1.26} catalyst (4,732.69 kg m⁻³) and *t* is the thickness of catalyst (~1 nm). The amorphous PtSe_x catalyst gives a Pt mass activity of 16.31 A mg_{Pt}⁻¹ at 20 mV versus RHE.

Macro-electrochemical measurements. The macro-electrochemical measurements were conducted on a glassy carbon electrode (3 mm in diameter), where the top of the rod (electrode surface) can be screwed off to facilitate the operation. Using a similar PMMA-assist transfer method to that described previously, we transferred an 0.5 × 0.5 cm² amorphous PtSe_x layer made from PtSe₂ grown by chemical vapour deposition on a glassy carbon electrode, and the sample area exceeding that of the glassy carbon electrode was scraped off before measurement (the atom-thin film's mass loading was 0.47 μg cm⁻²). A standard three-electrode cell was used, where a graphite (high purity) rod and a Ag/AgCl electrode served as the counter and reference electrodes, respectively. The measurements were conducted on a biological electrochemical station in a H₂-saturated 0.5 M H₂SO₄ solution. Linear sweep voltammetry was conducted at a

scan rate of 5 mV s^{-1} ; the onset potential is defined as the beginning potential of the Tafel linear region. The stability tests were carried out by two methods: continuous potential cycling in the potential window of -0.151 to -0.219 V versus RHE at a scan rate of 100 mV s^{-1} ; and a time-dependent overpotential (η) curve under $j = 20 \text{ mA cm}^{-2}$ and 140 mA cm^{-2} in $0.5 \text{ M H}_2\text{SO}_4$ aqueous solution. The current density was normalized by the geometric surface area of the electrode.

Preparation of IrO_x electrocatalyst. A titanium plate with a size of $2.5 \times 2.5 \text{ cm}^2$ was used as a substrate to deposit Ir. Prior to deposition, the Ti plate was ultrasonicated with acetone (3 min), isopropyl alcohol (3 min) and deionized water (3 min) to remove organic and inorganic contaminants on the surface, followed by N_2 blowing and drying. Then, the Ti plate was immediately loaded to the electron-beam evaporator with a base pressure of mid- 10^{-6} torr. A 50-nm-thick Ti layer was deposited as an adhesive layer, and 100-nm-thick Ir was deposited with a fixed deposition rate of 1.0 \AA s^{-1} . After deposition, the Ir/Ti plate was connected with Sn-Cu wire, and the edges were sealed by an epoxy (Hysol 9460). Then, the Ir/Ti plate was immersed in 1 M KOH solution for 1 hour, followed by continuous oxygen bubble formation by chronoamperometry to change iridium to iridium oxide and/or iridium hydroxide.

Electrochemical full-cell measurement. A two-electrode set-up was used to demonstrate the electrochemical full-cell measurement. A PtSe_x on FTO substrate was used as a working electrode. Prior to measurement, solution-processed SiO_x was deposited on the PtSe_x/FTO to promote the mechanical adhesion of wet-transferred PtSe_x on FTO. A thin SiO_x with thicknesses of 2, 5 and 10 nm was tested on the PtSe_x/FTO , and the 5 nm thickness of SiO_x showed the best current-potential characteristics. Details of preparation can be found in a reference³⁵. After SiO_x formation, the working electrode was connected with lead wire using Ag paste. The edges were sealed by an epoxy (Hysol 9460) except for an active area. An Ir/Ti electrocatalyst was used as a counter electrode. A working electrolyte was $0.5 \text{ M H}_2\text{SO}_4$ for hydrogen evolution and 1 M NaOH for oxygen evolution. An H-cell was used to carry out the full-cell measurement. Some 30 ml of aqueous electrolyte was filled in an individual cell, and a bipolar membrane (FuelCellStore) was utilized to separate the catholyte and anolyte. Before measurement, both electrolytes were purged with Ar for 30 min to eliminate unknown gas species. A BiStat (Bio-Logic) was used to take the two-electrode full-cell measurement with a scan rate of 20 mV s^{-1} .

Material characterizations. The microstructures and morphologies based on amorphous PtSe_x were characterized by optical microscopy, scanning electron microscopy (FEI 4200), Raman spectroscopy (WITec alpha300 R), micro-XPS (KRATOS-AXIS NOVA), XAS (Singapore Synchrotron Light Source) and STEM (JEOL ARM-200F (S)TEM equipped with CEOS CESCOR aberration corrector). The micro-electrochemical measurements were performed using two source meters (Keithley 2400 and 2450), synchronized by the general-purpose interface bus and the LabView script, allowing simultaneous recording of the electronic and electrochemical signals.

STEM imaging. The STEM imaging was operated at 80 kV acceleration voltage, and the beam was set to a convergence semi-angle of 28–33 mrad. HAADF imaging with the acquisition semi-angle of 68–280 mrad was employed to produce atomically resolved images whose intensity is approximately proportional to the square of the average atomic number Z of the material under investigation. This chemically sensitive Z -contrast mode is ideally suited to identify the nature of individual atoms directly. Regarding the cross-sectional STEM characterization, the freshly exfoliated PtSe_2 nanosheet was first treated by DRIE at a $\sim 50 \text{ s}$ duration to generate an amorphous monolayer surface. Then, this surface was covered by a MoS_2 flake for the subsequent focused ion beam milling process and STEM characterization. All the atomic-resolution HAADF STEM images presented here were filtered with a Wiener filter. Raman and XPS measurements were conducted on the mechanically exfoliated single-layer PtSe_2 samples with various plasma treatment times.

XPS measurement and fitting. The Pt-to-Se atomic ratio can be qualitatively determined by XPS measurement, based on the following relationship:

$$\frac{X_{\text{Pt}}}{X_{\text{Se}}} = \frac{I_{\text{Pt}4f}/\text{RSF}_{\text{Pt}4f}}{I_{\text{Se}3d}/\text{RSF}_{\text{Se}3d}} \quad (6)$$

where $I_{\text{Pt}4f}$ and $I_{\text{Se}3d}$ are the transmission-function-corrected peak area of the Pt 4f and Se 3d core-level spectra, respectively. The relative sensitivity factor (RSF) values for Pt 4f and Se 3d used in the calculation are 5.575 and 0.853, respectively. The peak areas are calculated by integrating the peaks over the energy range after background subtraction. All core-level spectra against the C 1s peak corresponding to the C-C group (284.8 eV) of adventitious carbon were first calibrated to obtain a precise fitting result. Then, the background-subtracted spectra with peaks were fitted by considering parameter constraints, such as peak width (full-width at half-maximum), energy separation, peak area ratio of the spin-orbit components and the Gaussian-Lorentzian character of the peaks.

Data availability

The data that support the plots within this paper or other findings of this study are available from the corresponding authors on reasonable request, or included in the published article and its Supplementary Information. Source data are provided with this paper.

Received: 25 March 2021; Accepted: 31 January 2022;
Published online: 10 March 2022

References

- Price pressures on metals. *Nat. Catal.* **2**, 735 (2019).
- Li, C. & Baek, J.-B. Recent advances in noble metal (Pt, Ru, and Ir)-based electrocatalysts for efficient hydrogen evolution reaction. *ACS Omega* **5**, 31–40 (2020).
- Zhang, Y. et al. Recent advances in one-dimensional noble-metal-based catalysts with multiple structures for efficient fuel-cell electrocatalysis. *Coord. Chem. Rev.* **450**, 214244 (2022).
- James, B. 2018 Cost Projections of PEM Fuel Cell Systems for Automobiles and Medium-Duty Vehicles https://www.energy.gov/sites/prod/files/2018/04/f51/fto_webinarslides_2018_costs_pem_fc_autos_trucks_042518.pdf (2018).
- Liu, M., Zhao, Z., Duan, X. & Huang, Y. Nanoscale structure design for high-performance Pt-based ORR catalysts. *Adv. Mater.* **31**, 1802234 (2019).
- Zhang, L., Doyle-Davis, K. & Sun, X. Pt-based electrocatalysts with high atom utilization efficiency: from nanostructures to single atoms. *Energy Environ. Sci.* **12**, 492–517 (2019).
- Xu, Y. & Zhang, B. Recent advances in porous Pt-based nanostructures: synthesis and electrochemical applications. *Chem. Soc. Rev.* **43**, 2439–2450 (2014).
- Chen, C. et al. Highly crystalline multimetallic nanoframes with three-dimensional electrocatalytic surfaces. *Science* **343**, 1339–1343 (2014).
- Funatsu, A. et al. Synthesis of monolayer platinum nanosheets. *Chem. Commun.* **50**, 8503–8506 (2014).
- Kijima, T. et al. Synthesis of nanohole-structured single-crystalline platinum nanosheets using surfactant-liquid-crystals and their electrochemical characterization. *Adv. Funct. Mater.* **19**, 545–553 (2009).
- Yin, H. et al. Ultrathin platinum nanowires grown on single-layered nickel hydroxide with high hydrogen evolution activity. *Nat. Commun.* **6**, 6430 (2015).
- Li, M. et al. Ultrafine jagged platinum nanowires enable ultrahigh mass activity for the oxygen reduction reaction. *Science* **354**, 1414–1419 (2016).
- Zhao, M. et al. Metal-organic frameworks as selectivity regulators for hydrogenation reactions. *Nature* **539**, 76–80 (2016).
- Jiang, K. et al. Single platinum atoms embedded in nanoporous cobalt selenide as electrocatalyst for accelerating hydrogen evolution reaction. *Nat. Commun.* **10**, 1743 (2019).
- Cheng, N. et al. Platinum single-atom and cluster catalysis of the hydrogen evolution reaction. *Nat. Commun.* **7**, 13638 (2016).
- Jiang, K. et al. Rational strain engineering of single-atom ruthenium on nanoporous MoS_2 for highly efficient hydrogen evolution. *Nat. Commun.* **12**, 1687 (2021).
- Toh, C.-T. et al. Synthesis and properties of free-standing monolayer amorphous carbon. *Nature* **577**, 199–203 (2020).
- Lee, S.-H., Kwak, E.-H. & Jeong, G.-H. Dewetting behavior of electron-beam-deposited Au thin films on various substrates: graphenes, quartz, and SiO_2 wafers. *Appl. Phys. A* **118**, 389–396 (2015).
- Li, H. et al. Activating and optimizing MoS_2 basal planes for hydrogen evolution through the formation of strained sulphur vacancies. *Nat. Mater.* **15**, 48–53 (2016).
- Lichtenstein, L. et al. The atomic structure of a metal-supported vitreous thin silica film. *Angew. Chem. Int. Ed.* **51**, 404–407 (2012).
- He, Y. et al. Self-gating in semiconductor electrocatalysis. *Nat. Mater.* **18**, 1098–1104 (2019).
- He, Y. et al. Engineering grain boundaries at the 2D limit for the hydrogen evolution reaction. *Nat. Commun.* **11**, 57 (2020).
- Jaramillo, T. F. et al. Identification of active edge sites for electrochemical H_2 evolution from MoS_2 nanocatalysts. *Science* **317**, 100–102 (2007).
- Li, Y. et al. MoS_2 nanoparticles grown on graphene: an advanced catalyst for the hydrogen evolution reaction. *J. Am. Chem. Soc.* **133**, 7296–7299 (2011).
- Wang, T. et al. High coverage CO activation mechanisms on Fe(100) from computations. *J. Phys. Chem. C* **118**, 1095–1101 (2014).
- Digne, M., Sautet, P., Raybaud, P., Euzen, P. & Toulhoat, H. Use of DFT to achieve a rational understanding of acid–basic properties of γ -alumina surfaces. *J. Catal.* **226**, 54–68 (2004).
- Li, H. et al. Synergetic interaction between neighbouring platinum monomers in CO_2 hydrogenation. *Nat. Nanotechnol.* **13**, 411–417 (2018).
- Han, N. et al. Nitrogen-doped tungsten carbide nanoarray as an efficient bifunctional electrocatalyst for water splitting in acid. *Nat. Commun.* **9**, 924 (2018).

29. Zhigang, S., Baolian, Y. & Ming, H. Bifunctional electrodes with a thin catalyst layer for 'unitized' proton exchange membrane regenerative fuel cell. *J. Power Sources* **79**, 82–85 (1999).
30. Altmann, S., Kaz, T. & Friedrich, K. A. Bifunctional electrodes for unitized regenerative fuel cells. *Electrochim. Acta* **56**, 4287–4293 (2011).
31. Perdew, J. P., Burke, K. & Ernzerhof, M. Generalized gradient approximation made simple. *Phys. Rev. Lett.* **77**, 3865–3868 (1996).
32. Hafner, J. Ab-initio simulations of materials using VASP: density-functional theory and beyond. *J. Comput. Chem.* **29**, 2044–2078 (2008).
33. Kresse, G. & Joubert, D. From ultrasoft pseudopotentials to the projector augmented-wave method. *Phys. Rev. B* **59**, 1758–1775 (1999).
34. He, Q. et al. In situ probing molecular intercalation in two-dimensional layered semiconductors. *Nano Lett.* **19**, 6819–6826 (2019).
35. Labrador, N. Y. et al. Enhanced performance of Si MIS photocathodes containing oxide-coated nanoparticle electrocatalysts. *Nano Lett.* **16**, 6452–6459 (2016).

Acknowledgements

This work was supported by the Singapore National Research Foundation Singapore programme (NRF-CRP21-2018-0007, NRF-CRP22-2019-0060, NRF-CRP18-2017-02 and NRF-CRP19-2017-01) and the Singapore Ministry of Education via AcRF Tier 3 (MOE2018-T3-1-002), AcRF Tier 2 (MOE2017-T2-2-136, MOE2019-T2-2-105 and MOE2018-T2-1-176) and AcRF Tier 1 (RG7/18 and 2019-T1-002-034). It was also supported by the National Key Research and Development Program of China (2019YFA0705400, 2021YFE0194200), the National Natural Science Foundation of China (11772153, 22073048, 21763024, 22175203, 22006023), the Natural Science Foundation of Jiangsu Province (BK20190018), the National Key R&D Program of China (2021YFA1500900), the Fundamental Research Funds for Central Universities (531119200209, NE2018002, NJ2020003) and the High-Performance Computing Center of Nanjing Tech University. Catalan Institute of Nanoscience and Nanotechnology (ICN2) acknowledges funding from Generalitat de Catalunya 2017SGR327 and the project NANOGEN (PID2020-116093RB-C43), funded by MCIN/AEI/10.13039/501100011033/. ICN2 is supported by the Severo Ochoa programme from Spanish MINECO (grant no. SEV-2017-0706) and is funded by the CERCA Programme/Generalitat de Catalunya. This work has received funding from the European Union's Horizon 2020 research and innovation programme under grant agreement no.

823717-ESTEEM3. P.T. acknowledges Humboldt Research Fellowship for Postdoctoral Researchers sponsored by the Alexander von Humboldt Foundation. We thank S. Teddy (School of Materials Science and Engineering, Nanyang Technological University, Singapore) for XPS data analysis.

Author contributions

Z.L. and Y.H. conceived and initiated the project. Z.L. and Z. Zhang supervised the project and led the collaboration efforts. Y.H. designed the experiments, synthesized the PtSe₂ films and performed the micro-/macro-electrochemical HER measurement. C.Z. (0000-0001-6383-3665), P.T., X.Z., M.H., R.E.D.-B. and J.A. performed the TEM, STEM and cross-sectional STEM measurements. Z. Zhang, L.L., W.G. and Z. Zhao performed atomistic computations and theoretical analyses. B.K. and B.S. did the electrolyser-cell measurements. P.G., S.G., M.X., C.Z. (0000-0002-1589-855X), X.W., L.Z., Z.S., C.G., J.Y. and H.D. assisted with the material characterizations, device fabrication and chemical vapour deposition synthesis. Y.D. conducted the XAS measurement. P.Y. helped with the synthesis of PtSe₂ single crystal by the chemical vapour transport (CVT) method. Y.H., L.L., Q.J.W., Z. Zhang and Z.L. wrote the paper. All authors discussed the results and commented on the manuscript.

Competing interests

The authors declare no competing interests.

Additional information

Supplementary information The online version contains supplementary material available at <https://doi.org/10.1038/s41929-022-00753-y>.

Correspondence and requests for materials should be addressed to Yongmin He, Qi Jie Wang, Zhuhua Zhang or Zheng Liu.

Peer review information *Nature Catalysis* thanks the anonymous reviewers for their contribution to the peer review of this work.

Reprints and permissions information is available at www.nature.com/reprints.

Publisher's note Springer Nature remains neutral with regard to jurisdictional claims in published maps and institutional affiliations.

© The Author(s), under exclusive licence to Springer Nature Limited 2022